Dec. 2019 Transactions of Nanjing University of Aeronautics and Astronautics Vol. 36 No. 6

A Laser Line Scanner Based Hole Position Correction Mechanism for Automatic Drilling and Riveting in Aircraft Assembly

ZHANG Lin[1*], *TIAN Wei*[1], *SUN Hailong*[2], *XUE Qiwei*[1], *LIU Yangyang*[1],
LIAO Wenhe[3]

1. College of Mechanical & Electrical Engineering, Nanjing University of Aeronautics and Astronautics, Nanjing 210016, P. R. China;
2. Laboratory of Aeronautics Intelligent Equipment Technology Research, AVIC Chengdu Aircraft Industry (Group) Co., Ltd., Chengdu 610092, P. R. China;
3. School of Mechanical Engineering, Nanjing University of Science and Technology, Nanjing 210094, P. R. China

(Received 31 October 2018; revised 25 November 2019; accepted 15 December 2019)

Abstract: The low-stiffness of aircraft skins may results in the differences between aircraft actual parts and their theoretical models, which will consequently affect the accuracy of automatic drilling and riveting in aircraft assembly. In this paper, a novel approach of hole position correction using laser line scanner (LLS) is proposed to assign a single row of holes on the parts' surfaces. First, we adopt a space circle fitting method and the random sample consensus (RANSAC) to obtain the precise coordinates of center of the datum holes' coordinates. Second, LLS is calibrated by the laser tracker, and the relations between the LLS coordinate system and the tool coordinate system (TCS) can be calculated. Third, the kinematics model of the automatic riveting machine is established based on a two-point referencing strategy proposed in this paper. Thus, the positions of the holes to be drilled can be adjusted. Finally, the experimental results show that in TCS the measurement error of LLS is less than 0.1 mm, and the correction error of the hole position is less than 0.5 mm, which demonstrates the reliability of our method.

Key words: aircraft assembly; automatic drilling and riveting system (ADRS); laser line scanner (LLS); position correction

CLC number: V261.97 **Document code**: A **Article ID**: 1005-1120(2019)06-0952-12

0 Introduction

Assembly automation has been progressing in aerospace industry for nearly a decade. Driven by commercial requirements, airspace automation has primarily counted on automated drilling and riveting machines to reduce cost and improve quality, which has hence boosted the advancement of automatic drilling and riveting systems (ADRSs). For example, the leading aerospace automation company, ELECTROIMPACT, has customized a robotic drilling system for Airbus[1] , and its archrival, BROETJE-Automation, has developed a mobile robot based drilling and fastening system for multi uses in aircraft assembly automation[2]. Despite the efficiency ADRSs are brought out, a critical problem remains the drilling process. Modern aircraft skins coming to assembly usually hold a low stiffness, and their shapes might differ from their theoretical models forged by computer aided design (CAD)[3]. Positioning holes to be drilled on those materials inevitably lead to deviations. Typically, two terms are used to describe these variations: position error, referring to the deviation between the coordinates of

---

*Corresponding author, E-mail address: zhanglin05@nuaa. edu. cn.

How to cite this article: ZHANG Lin, TIAN Wei, SUN Hailong, et al. A Laser Line Scanner Based Hole Position Correction Mechanism for Automatic Drilling and Riveting in Aircraft Assembly[J]. Transactions of Nanjing University of Aeronautics and Astronautics, 2019,36(6):952-963.
http://dx.doi.org/10.16356/j.1005-1120.2019.06.008

a hole in theoretical models and those in actual parts; and orientation error, regarding the difference between the normal vector of a part's surface and the spindle axis of the tool.

Researchers have adopted different approaches to address this issue, including laser range sensors[4-5], monocular vision and stereo cameras. Shi et al.[6] designed an intelligent normal adjustment cell for hole-drilling end effectors by using a double-eccentric disk normal adjustment mechanism and a spherical plain bearing. Although their approach was proved capable of improving hole-drilling quality, it could achieve an adjustment only within ±5° and is too complicated to be installed on certain existing end effectors. Yu et al.[7] deployed four laser displacement sensors to measure surface normal errors in a fast and simple way, but without considering position errors. Zhu et al.[8-10] developed a 2D vision system for hole-positioning accuracy and investigated the principles of error measurement and error compensation for robotic drilling. Their research demonstrated that measurement accuracy could be enhanced if both the perpendicularity of the camera optical axis to the workpiece surface and the object distance are properly maintained during the measurement process, albeit in a time-consuming way. Wang et al.[11] utilized the visual measurement system to detect and correct installation error between workpiece and the robot drilling system, and devised an effective approach of calibrating an base detection.

More than measurement systems, many studies have devoted to reference strategies. Zhu et al.[12] used bilinear interpolation models to correct the hole position according to measurement data of reference holes. Sumeihl et al.[13] discussed different optical reference strategies, including the three-point geometric strategy, the multi-point geometric strategy, the multi-point best-fit strategy and the static helper-frame strategy.

In this paper, a novel approach was proposed to measure datum holes for the ADRS. In Section 1 the architecture of the ADRS was briefly described. Then, Section 2 presented the measurement system with LLS. The calibration method of LLS was described in Section 3. The referencing strategy was introduced in Section 4. The experiments were introduced, and some results were shown in Section 5.

1 Automatic Drilling and Riveting System

A functional ADRS consists of five components: a five-axis machine tool, a MFEE, ground rails, a rotary table and an aircraft part, as shown in Fig. 1(a)[14]. The part is fixed on a rotary table, which can spin around 360°. The five-axis machine tool moves along the linear ground rails. The independently developed MFEE is installed on the ram of the machine tool and can approach the part from all directions.

MFEE, the essence of ADRS, involves several modules, as shown in Fig.1(b), to complete different functions, like clamping pressure foot, drilling holes, feeding nails, riveting, etc. All these processes are controlled by a programmable logic controller (PLC). MFEE also incorporates different sensors, like laser displacement sensors, a laser line scanner (LLS), length gauges and electromagnetic proximity sensors, to guide those processes. For example, the four laser displacement sensors measure surface-normal of the part and adjust MFEE to be perpendicular to the surface of the part for hole-drilling.

The whole system is operated through dedicated software, and follows a workflow that includes two critical tasks: measurement and correction.

(1) Numerical control (NC) codes, generated by off-line program based on the CAD model, are input into the control software.

(2) The machine tool drives MFEE to the position of the datum hole.

(3) LLS scans the pre-drilling datum hole and obtains its coordinates.

(4) The actual drilling position is calculated by using the deviation between the coordinates of the datum hole in CAD model and those that LLS obtains in (3).

(5) The machine tool drives MFEE to the calculated drilling position.

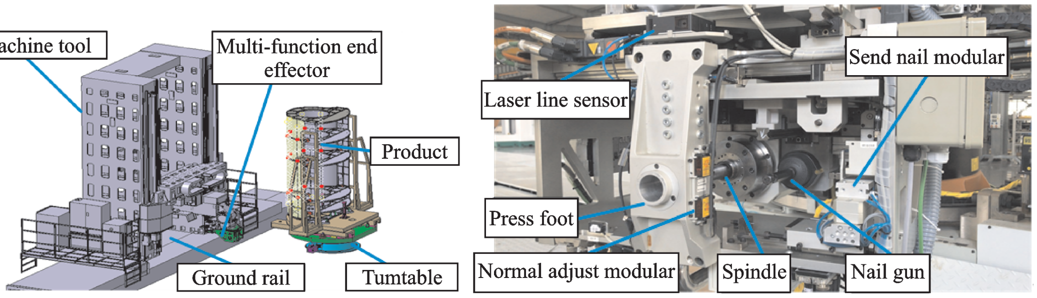

(a) Assembly on-site (b) Multi-function end effector

Fig.1 Automatic drilling and riveting system

(6) MFEE performs drilling and riveting.

2 Measurement

2.1 Mechanism for scanning the datum hole

Fig. 2 explains the mechanism of scanning the datum hole. A LLS is mounted on a high-precision linear guide and driven by a servo motor. The LLS measures range and direction to reflect the surface of an object with high precision. The data it gleans are transformed into the sensor coordinate system (SCS), that is, Y and Z coordinates, while the value on X axis is the distance the LLS travels along the linear guide, which can be read through the motor controller. Thus, the 3D surface of the part can be plotted through measurement.

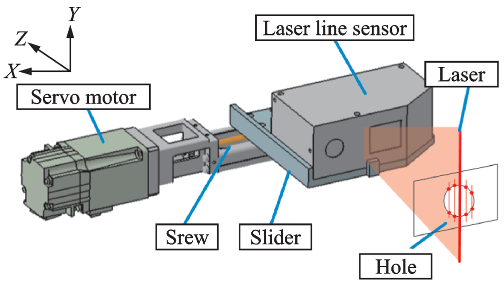

Fig.2 Mechanism for scanning the datum hole

Table 1 lists LLS's key parameters. The measuring range of the LLS is within a square of 25 mm×25 mm, and the servo motor moves within a length of 25 mm. The datum hole usually holds a diameter of 3—4 mm, which falls within the measuring range given the assembly error less than 10 mm. The LLS bears a resolution of 2 μm on both Y and Z directions, and the motor has a 1 μm resolution on X direction, which results in a synthetic resolution of $\sqrt{2^2+2^2+1^2}=3$ μm, catering to the measurement demand.

Table 1 Parameters of the laser line scanner

Direction	Parameter	Value
Z-axis	Start of measuring range/mm	53.5
	End of measuring range/mm	78.5
	Height of measuring range/mm	25.0
	Reference resolution/μm	2
Y-axis	Start of measuring range/mm	−12.5
	End of measuring range/mm	+12.5
	Height of measuring range/mm	25.0
	Reference resolution	1 280 points (2 μm)

2.2 Circle fitting algorithm

2.2.1 Obtaining edge points

The LLS obtains 1 280 points to describe a profile. Fig.3 shows the coordinates of all the points of a profile, where the two edge points can be clearly identified. In order to obtain the two points, we adopt a point-by-point comparison method.

$$\begin{cases}\text{Left: }\left|z_i-z_{i-1}\right|\approx 0 \text{ and } \left|z_i-z_{i+1}\right|>\varepsilon \\ \text{Right: }\left|z_i-z_{i-1}\right|>\varepsilon \text{ and } \left|z_i-z_{i+1}\right|\approx 0\end{cases} \tag{1}$$

where i is the index from 1 to 1 280 and ε the thresh-

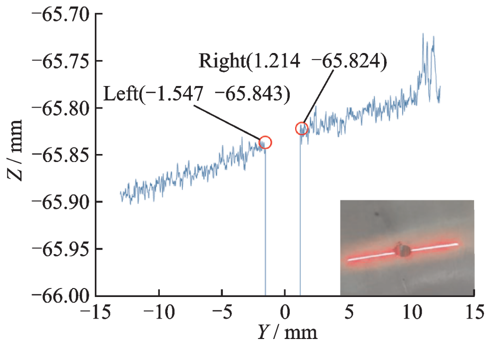

Fig.3 Coordinates of the 1 280 points of a profile

old for comparison. Eq.(1) implies that the left edge point is the one whose Z coordinate is almost the same as that of its immediate predecessor, but much larger than that of its immediate successor; while the right edge point follows a complete opposite rule. If the laser line misses the hole, there is no edge point.

2.2.2 Plane fitting

As the motor is moving, a series of points can be obtained and regarded as locating on the circumference of the hole. A hole with a diameter of 4 mm might provide about 50 points. The circle fitting algorithm was used to calculate its center.

Suppose there is a set of points $\boldsymbol{P}\{p_1, p_2, \cdots, p_n\}$, where all the points are on a same plane denoted as π. Each point P_i in $\boldsymbol{P}$ satisfies

$$ax_i + by_i + cz_i = 1 \tag{2}$$

where (x_i, y_i, z_i) represent the coordinates of point P_i, and (a, b, c) the normal of π, which can determine a plane.

If $\boldsymbol{P}$ includes n points there are n equations like Eq.(2) and they can be unified as

$$\boldsymbol{PN} = \boldsymbol{l} \tag{3}$$

where $\boldsymbol{P} = \begin{bmatrix} x_1 & y_1 & z_1 \\ x_2 & y_2 & z_2 \\ \vdots & \vdots & \vdots \\ x_n & y_n & z_n \end{bmatrix}, \boldsymbol{N} = \begin{bmatrix} a \\ b \\ c \end{bmatrix}, \boldsymbol{l} = \begin{bmatrix} 1 \\ 1 \\ \vdots \\ 1 \end{bmatrix}$. $\boldsymbol{N}$ can be obtained through the least square method (LSM), shown as

$$\boldsymbol{N} = (\boldsymbol{P}^{\mathrm{T}}\boldsymbol{P})^{-1}\boldsymbol{P}^{\mathrm{T}}\boldsymbol{l} \tag{4}$$

Then $\boldsymbol{N}$ can be normalized by Eq.(5)

$$\boldsymbol{N} = (a_n, b_n, c_n) = \frac{(a, b, c)}{\sqrt{a^2 + b^2 + c^2}} \tag{5}$$

2.2.3 Project of the point set onto the plane

Since no equation is available to describe a circle in 3D space, we have to fit the scanned points into a 2D circle to find the hole center. Therefore, we can project the points in set $\boldsymbol{P}$ onto plane π, and the projected points compose a set $\boldsymbol{P}'\{p'_1, p'_2, \cdots, p'_n\}$. Fig.4 displays the projection results, where the solid dots represent the points in $\boldsymbol{P}$, and the hollow dots represent the projected points.

Denote the distance between p_i and p'_i as d_i.

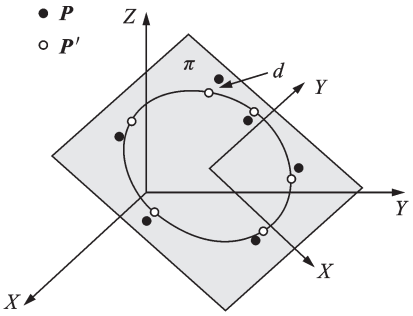

Fig.4 Projection of scanned points onto plane π

Then $p'_i(x'_i, y'_i, z'_i)$ can be expressed as

$$\begin{cases} x'_i = a_n d_i + x_i \\ y'_i = b_n d_i + y_i \\ z'_i = c_n d_i + z_i \end{cases} \tag{6}$$

Since p'_i is just on the plane π, it satisfies the Eq.(2). Thus, substituting p'_i into Eq.(2), we have

$$a(a_n d_i + x_i) + b(b_n d_i + y_i) + c(c_n d_i + z_i) = 1 \tag{7}$$

Therefore, d_i can be obtained

$$d_i = \frac{|ax_i + by_i + cz_i - 1|}{\sqrt{a^2 + b^2 + c^2}} \tag{8}$$

Then, substitute d_i into Eq.(6), we can obtain $p'_i(x'_i, y'_i, z'_i)$.

2.2.4 Transformation of a 3D circle into a 2D circle

Assume that $\boldsymbol{Q}\{q_1, q_2 \cdots q_n\}$ is a set of points on the plane xoy, $\boldsymbol{Q}$ can be transformed into $\boldsymbol{P}'$ through two steps: $\boldsymbol{Q}$ first rotates around the X axis and then rotates around the Y axis, that is

$$\boldsymbol{Q} = {}^{Q}_{P'}\boldsymbol{T}\boldsymbol{P}' \qquad {}^{Q}_{P'}\boldsymbol{T}^{-1} = {}^{Q}_{P'}\boldsymbol{T} \tag{9}$$

The transformation matrix from $\boldsymbol{Q}$ to $\boldsymbol{P}'$ is

$$\begin{gathered} {}^{Q}_{P'}\boldsymbol{T} = \mathrm{Rot}(x, \alpha)\mathrm{Rot}(y, \beta) = \\ \begin{bmatrix} 1 & 0 & 0 \\ 0 & \cos\alpha & -\sin\alpha \\ 0 & \sin\alpha & \cos\alpha \end{bmatrix} \times \begin{bmatrix} \cos\beta & 0 & \sin\beta \\ 0 & 1 & 0 \\ -\sin\beta & 0 & \cos\beta \end{bmatrix} = \\ \begin{bmatrix} \cos\beta & 0 & \sin\beta \\ \sin\alpha\sin\beta & \cos\alpha & -\sin\alpha\cos\beta \\ -\cos\alpha\sin\beta & \sin\alpha & \cos\alpha\cos\beta \end{bmatrix} \end{gathered} \tag{10}$$

Since the normal of plane π is (a_n, b_n, c_n), Eq.(11) is obtained

$$\begin{cases} a_n = \sin\beta \\ b_n = -\sin\alpha\cos\beta \\ \mathrm{c}_n = \cos\alpha\cos\beta \end{cases} \tag{11}$$

Thus

$$\begin{cases}\beta = \arcsin a_n \\ \alpha = \arccos \dfrac{c_n}{\cos\beta}\end{cases} \tag{12}$$

Substituting α and β into Eq.(9) and Eq.(10), we can obtain ${}^{Q}_{P'}\boldsymbol{T}$ and $\boldsymbol{Q}$.

2.2.5 2D circle fitting

The equation of 2D circle is expressed as

$$x^2 + y^2 + Dx + Ey + F = 0 \tag{13}$$

Since point $q_i(x_i'', y_i'', 0)$ satisfies Eq.(13), and is included in set $\boldsymbol{Q}$, we have

$$\boldsymbol{AB} = \boldsymbol{m} \tag{14}$$

where $\boldsymbol{A} = \begin{bmatrix} x_1'' & y_1'' & 1 \\ x_2'' & y_2'' & 1 \\ \vdots & \vdots & \vdots \\ x_i'' & y_i'' & 1 \end{bmatrix}$, $\boldsymbol{B} = \begin{bmatrix} D \\ E \\ F \end{bmatrix}$, $\boldsymbol{m} = \begin{bmatrix} -x_1''^2 - y_1''^2 \\ -x_2''^2 - y_2''^2 \\ \vdots \\ -x_i''^2 - y_i''^2 \end{bmatrix}$. Eq.(14) can be solved by LSM

$$\boldsymbol{B} = (\boldsymbol{A}^{\mathrm{T}}\boldsymbol{A})^{-1}\boldsymbol{P}^{\mathrm{T}}\boldsymbol{m} \tag{15}$$

Then, the center of the 2D circle outlined by points in set $\boldsymbol{Q}$ is

$$O''(x_o'', y_o'', 0) = \left(-\frac{D}{2}, -\frac{E}{2}, 0\right) \tag{16}$$

And its radius is

$$r = \frac{\sqrt{D^2 + E^2 - 4F}}{2} \tag{17}$$

The center of the 3D circle delineated by points in set $\boldsymbol{P}$ is denoted as $O(x_o, y_o, z_o)$, and O can be calculated as

$$O = {}^{P'}_{Q}TO'' \tag{18}$$

Thus, center and radius of the 3D circle are obtained by coordinate transformation and the fitting algorithm.

2.3 RANSAC method

Section 2.2 describes an ideal situation where the circle fitting algorithm could perform. In the real world, not all the points in set $\boldsymbol{P}$ fall exactly on the circumference of the hole, given the burrs and scratches that often emerge on the surface. The outliers may severely interfere the results of fitting. Therefore, we adopt random sample consensus (RANSAC) to filter the outliers. The filtering steps are as follows.

(1) Randomly select 4—5 points from the original point set $\boldsymbol{P}$ to compose a subset called the hypothetical inliers H.

(2) Fit a 3D circle of the points in H by using the method described in Section 2.2. The resulted model includes a circle with a center of $O^h(x_o^h, y_o^h, z_o^h)$, and a radius of r^h, and a plane π^h.

(3) Calculate the key parameters revealing relative positions between the model and each of the rest points in $\boldsymbol{P}$ through Eq.(19)

$$\begin{cases} R_i = \sqrt{(x_i - x_o^h)^2 + (y_i - y_o^h)^2 + (z_i - z_o^h)^2} \\ D_i = \dfrac{|ax_i + by_i + z_i - 1|}{\sqrt{a^2 + b^2 + c^2}} \end{cases} \tag{19}$$

where R_i represents the distance between point p_i to the center of the circle and D_i the distance between p_i and plane π^h.

(4) Determine whether the rest points fit the estimated model by

$$R_i < R_{\mathrm{t}} \qquad D_i < D_{\mathrm{t}} \tag{20}$$

where R_{t} is the threshold in radial direction, and D_{t} the threshold in normal direction of π^h. If a point satisfies Eq.(20), it is included into the consensus set.

(5) If sufficient points are included in the consensus set, say 80% of the rest in $\boldsymbol{P}$, the fitted model is regarded as reasonably good and the filtering proceeds to the next step; otherwise, it goes back to (1) and starts with reselecting H.

(6) Improve the fitted model by re-estimating it using all the points in the consensus set.

3 Sensor Calibrations

3.1 Establishment of tool coordinate system

Tool coordinate system (TCS), denoted by \$Tool, is convenient for numerical control to determine the machine's positions and attitudes. We introduce a laser tracker with an accuracy of 0.025 mm to establish a TCS. The target ball of the laser tracker is mounted on the tool holder of the spindle through a fixture, as shown in Fig.5.

Thus, the origin of the TCS is the center of the target ball, which is 10 mm away from the press foot plane. The TCS consists of the Z-axis that is along the feed direction of the spindle, the vertical

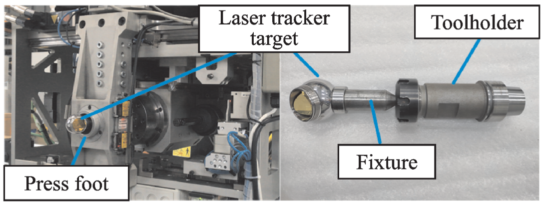

Fig.5 Installation of the target ball of the laser tracker

Y-axis and the horizontal X-axis. This definition of TCS is close to that of the machine coordinate system (MCS), which will benefit numerical control.

Fig. 6 explains the TCS, where the red dots are those measured by the laser tracker. The establishment of TCS is as follows.

(1) Stick the target ball onto the surface of press foot and move it, thus the laser tracker could measure a series of points. Use these points to fit a plane, and denote it as π_P.

(2) Fix the target ball on the spindle. Adjust the feed motor by using the laser tracker to ensure the 10 mm distance between the center of the target ball and plane π_P. Then set the center of the target ball as the origin of TCS.

(3) Move the machine tool along the X-axis of MCS, and the laser tracker captures the trajectory of the center of the target ball, that is, a straight line denoted as l_x.

(4) Move the machine tool along the Y-axis of MCS, and the laser tracker measures the trajectory of the center of the target ball, l_y.

(5) Define the line passing through the origin and parallel to l_x as the X-axis of TCS, and the line perpendicular to the plane where l_x and l_y cross as the Z-axis. Thus the Y-axis is defined by the right-hand rule.

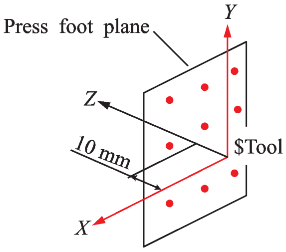

Fig.6 Tool coordinate system

3.2 Calibration process

The points scanned by LLS are endowed with the coordinates on the sensor coordinate system (SCS), denoted as \$Sensor, which have to be transformed to those on the TCS. But the exact position of LLS cannot be determined in advance given the installation error. Therefore, the transformation must be precisely calibrated

$$ {}_{T}^{S}\boldsymbol{T}=\begin{bmatrix} {}_{T}^{S}\boldsymbol{R} & {}_{T}^{S}\boldsymbol{t} \\ 0 & 1 \end{bmatrix} \tag{21} $$

where ${}_{T}^{S}\boldsymbol{T}$ is the transformation matrix, ${}_{T}^{S}\boldsymbol{R}$ the rotation matrix of 3×3, and ${}_{T}^{S}\boldsymbol{t}$ the translation vector of 3×1.

There is a fixed calibration board with a smooth hole, as depicted in Fig.7.

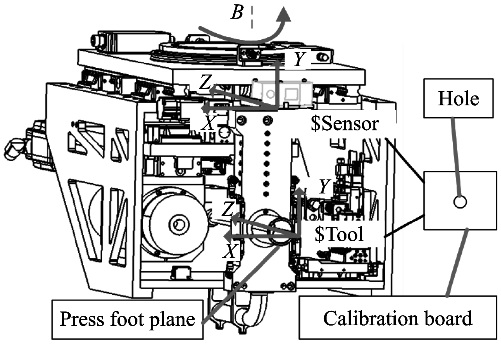

Fig.7 Sensor calibration

The hole is within the measurement range of LLS. Thus, the SCS coordinates of the hole, denoted as p^s, can be obtained by the method described in Section 2.3, while the TCS coordinates of it, denoted as p^t, can be measured by the laser tracker. After several experiments, two point sets $P^s\{p_1^s, p_2^s, \cdots, p_n^s\}$ and $P^t\{p_1^t, p_2^t, \cdots, p_n^t\}$ can be obtained, where p_i^s and p_i^t hold the following relation

$$ p_i^t = {}_{S}^{T}\boldsymbol{R}p_i^s + {}_{S}^{T}\boldsymbol{t} \tag{22} $$

The calculation methods of ${}_{S}^{T}\boldsymbol{R}$ and ${}_{S}^{T}\boldsymbol{t}$ are as follows[14]

(1) Calculate the average of P^s and P^t

$$ \begin{cases} \overline{p^s} = \dfrac{1}{n}\sum\limits_{i=1}^{n} p_i^s \\ \overline{p^t} = \dfrac{1}{n}\sum\limits_{i=1}^{n} p_i^t \end{cases} \tag{23} $$

(2) Calculate $p_i^s{}'$ and $p_i^t{}'$

$$\begin{cases} p_i^s{}' = p_i^s - \overline{p^s} \\ p_i^t{}' = p_i^t - \overline{p^t} \end{cases} \tag{24}$$

(3) Calculate the 3 × 3 matrix $\boldsymbol{H}$

$$\boldsymbol{H} = \sum_{i=1}^{n} p_i^s{}' p_i^t{}'^{\mathrm{T}} \tag{25}$$

(4) Find the SVD of $\boldsymbol{H}$

$$\boldsymbol{H} = \boldsymbol{U}\Lambda\boldsymbol{V}^{\mathrm{T}} \tag{26}$$

(5) Calculate ${}_S^T\boldsymbol{R}$

$${}_S^T\boldsymbol{R} = \boldsymbol{V}\boldsymbol{U}^{\mathrm{T}} \tag{27}$$

(6) Calculate ${}_S^T\boldsymbol{t}$

$${}_S^T\boldsymbol{t} = \overline{p^t} - {}_S^T\boldsymbol{R}\,\overline{p^s} \tag{28}$$

Therefore, the transformation between the two systems can be described as assume that the datum hole measured by LLS in TCS, and can be expressed as

$$\begin{cases} O^t = {}_S^T\boldsymbol{T}O^s \\ n^t = {}_S^T\boldsymbol{R}n^s \end{cases} \tag{29}$$

where (O^s, n^s) is the SCS coordinate pair of the position and the orientation of a hole, and (O^t, n^t) its counterpart in TCS.

4 Referencing Strategy

4.1 Kinematic model

Fig.8 explains the structure of the five-axis machine tool. It consists of three linear axes X, Y and Z, and two rotary axes A and B, which rotate about the X-axis and the Y-axis, respectively.

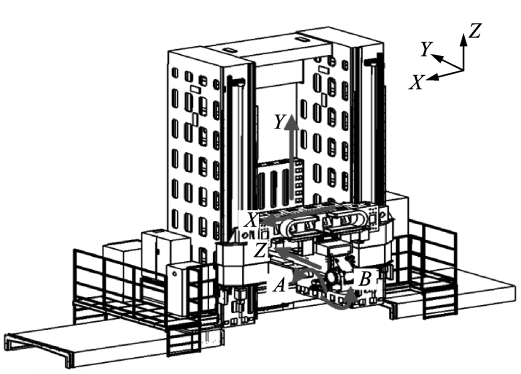

Fig.8 Structure of the machine tool

The MCS, denoted as \$Base, is a base coordinate system fixed to the machine tool body, as outlined in Fig.9. The three lines in Fig.9, rotary centerline of the A-axis, rotary centerline of the B-axis, and feed line of the spindle, can be measured by the laser tracker. Initially, the three lines are perpendicular to each other, and the coordinate system composed of the X-axis, the Y-axis, the Z-axis and the A-axis is coincident with the MCS. In Fig.9, l_1 denotes the distance between the two rotary centers of A-axis and B-axis, and l_2, l_3 and l_4 are annotated as well. The transfer chain of machine tool is as[15]: \$Base→\$$X$→\$$Y$→\$$Z$→\$$A$→\$$B$→\$Tool.

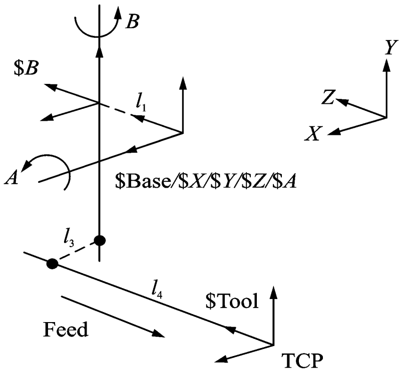

Fig.9 Coordinate systems of the machine tool

According to the rigid body model, relation between the MCS and the TCS can be modeled as

$${}_{\mathrm{Tool}}^{\mathrm{Base}}T = {}_X^{\mathrm{Base}}T\,{}_Y^XT\,{}_Z^YT\,{}_A^ZT\,{}_B^AT\,{}_{\mathrm{Tool}}^BT \tag{30}$$

where

$${}_X^{\mathrm{Base}}T = \begin{bmatrix} 1 & 0 & 0 & X_a - l_3 \\ 0 & 1 & 0 & 0 \\ 0 & 0 & 1 & 0 \\ 0 & 0 & 0 & 1 \end{bmatrix}$$

$${}_Y^XT = \begin{bmatrix} 1 & 0 & 0 & 0 \\ 0 & 1 & 0 & Y_a - l_2 \\ 0 & 0 & 1 & 0 \\ 0 & 0 & 0 & 1 \end{bmatrix}$$

$${}_Z^YT = \begin{bmatrix} 1 & 0 & 0 & 0 \\ 0 & 1 & 0 & 0 \\ 0 & 0 & 1 & Z_a - l_1 - l_4 \\ 0 & 0 & 0 & 1 \end{bmatrix}$$

$${}_A^ZT = \begin{bmatrix} 1 & 0 & 0 & 0 \\ 0 & \cos A_a & -\sin A_a & 0 \\ 0 & -\sin A_a & \cos A_a & 0 \\ 0 & 0 & 0 & 1 \end{bmatrix}$$

$${}_B^AT = \begin{bmatrix} \cos B_a & 0 & \sin B_a & 0 \\ 0 & 1 & 0 & 0 \\ -\sin B_a & 0 & \cos B_a & l_1 \\ 0 & 0 & 0 & 1 \end{bmatrix}$$

$$
{}^{B}_{\mathrm{Tool}}T=\begin{bmatrix}1 & 0 & 0 & l_3\\ 0 & 1 & 0 & l_2\\ 0 & 0 & 1 & l_4\\ 0 & 0 & 0 & 1\end{bmatrix}
$$

The third column of the matrix ${}^{\mathrm{Base}}_{\mathrm{Tool}}T$ identifies the Z-axis of TCS relative to MCS. The forth column identifies the origin of TCS, which is also tool tip point (TCP). Assume that $(x_g, y_g, z_g, i_g, j_g, k_g)$ is the position and the direction of the tool tip in MCS, we have

$$
\begin{cases}
i_g=\sin B_a\\
j_g=-\sin A_a\cos B_a\\
k_g=\cos A_a\cos B_a\\
x_g=l_3\cos B_a+l_4\sin B_a+X_a-l_3\\
y_g=l_3\sin A_a\sin B_a+l_2\cos A_a-\\
\qquad l_4\sin A_a\cos B_a+Y_a-l_1\sin A_a-l_2\\
z_g=-l_3\sin B_a\cos A_a+l_4\cos A_a\cos B_a+\\
\qquad l_2\sin A_a+Z_a+l_1\cos A_a-l_1-l_4
\end{cases}
\tag{31}
$$

Solving Eq.(31), we can obtain the inverse kinematics as

$$
\begin{cases}
A_a=-\arctan\dfrac{k_g}{j_g}\\
B_a=\arcsin i_g\\
X_a=x_g-l_3\cos B_a-l_4\sin B_a\\
Y_a=y_g-l_3\sin A_a\sin B_a-l_2\cos A_a+\\
\qquad l_4\sin A_a\cos B_a+l_1\sin A_a\\
Z_a=z_g+l_3\sin B_a\cos A_a-l_2\sin A_a+l_1-\\
\qquad l_4\cos A_a\cos B_a-l_1\cos A_a+l_4
\end{cases}
\tag{32}
$$

The transformation matrix ${}^{\mathrm{Base}}_{\mathrm{Tool}}T$ consists of a 3×3 homogeneous rotation matrix ${}^{\mathrm{Base}}_{\mathrm{Tool}}\boldsymbol{R}$ and a 3×1 translation vector ${}^{\mathrm{Base}}_{\mathrm{Tool}}\boldsymbol{t}$, as described in Eq.(33)

$$
{}^{\mathrm{Base}}_{\mathrm{Tool}}T=\begin{bmatrix}{}^{\mathrm{Base}}_{\mathrm{Tool}}\boldsymbol{R} & {}^{\mathrm{Base}}_{\mathrm{Tool}}\boldsymbol{t}\\ 0 & 1\end{bmatrix}
\tag{33}
$$

Given the TCS coordinates (O^t, n^t), the position and the orientation of the datum hole measured by LLS, the position and the orientation of any hole, denoted by (R^a, n^a), in MCS can be calculated as

$$
\begin{cases}
R^a={}^{\mathrm{Base}}_{\mathrm{Tool}}T\quad O^s\\
n^a={}^{\mathrm{Base}}_{\mathrm{Tool}}\boldsymbol{R}\quad n^s
\end{cases}
\tag{34}
$$

4.2 Two-point strategy

A group of rivets that fasten an aircraft part and the frame together might be roughly distributed along a straight line, usually following a narrow stringer. But given the assembly errors, the theoretical positions of the holes might deviate from the stringer. Therefore, holes at both ends of the line are used as datum, which will be drilled in advance, and others will be adjusted according to the datum holes.

Fig.10 presents the referencing strategy, including translating, rotating, and scaling transformation between theoretical and actual parts, where the solid black spots represent the datum holes, and the hollow circles represent the holes need to be drilled.

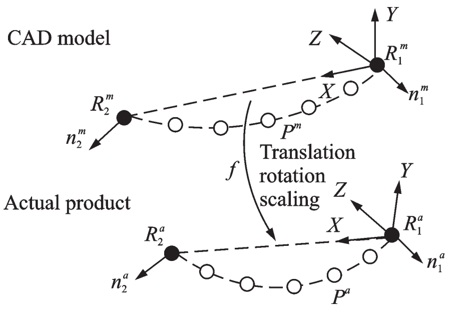

Fig.10 Principle of referencing strategy

By establishing local coordinate system (LCS), mapping between the theoretical model and the actual part can be created. The LCS can be established through two datum holes. Its origin and the base vectors can be described as

$$
\begin{cases}
\boldsymbol{x}=\dfrac{R_2-R_1}{|R_2-R_1|}\\
l_y=\dfrac{n_2\times n_1}{|n_2\times n_1|}\\
\boldsymbol{z}=\boldsymbol{x}\times l_y\\
\boldsymbol{y}=\boldsymbol{z}\times\boldsymbol{x}\\
\mathrm{origin}=R_1
\end{cases}
\tag{35}
$$

where R_i denotes coordinates of a datum hole, and n_i the orientation of a datum hole. The LCS's origin is on R_1 and its X-axis is coincident with $\boldsymbol{R}_1\boldsymbol{R}_2$. Cross-product $n_2\times n_1$ is nearly parallel to Y-axis.

The LCS can be established in both CAD model (denoted as \$Model) and on the actual part (denoted as \$Real). If the theoretical positions of the holes to be drilled in the CAD model are set as P^m, their LCS-\$Model coordinates L^m can be calculated as

$$L^m = [\,x^m \quad y^m \quad z^m\,](P^m - R_1^m) \tag{36}$$

The scaling factor between two LCSs can be defined as

$$f = \frac{\overline{R_1^a R_2^a}}{R_1^m R_2^m} \tag{37}$$

Then the LCS-$Real coordinates are

$$L^a = fL^m \tag{38}$$

Thus the corrected drilling position P^a is obtained as

$$P^a = R_1^a + [\,x^a \quad y^a \quad z^a\,]\,L^a \tag{39}$$

Adjusting the normal vector before drilling does not change the orientation of the holes to be drilled, and they remain the theoretical values, that is

$$n^a = n^m \tag{40}$$

Finally, on base of inverse kinematics, the joint coordinates of machine tools can be determined.

Fig.11 elaborates the whole procedure of referencing.

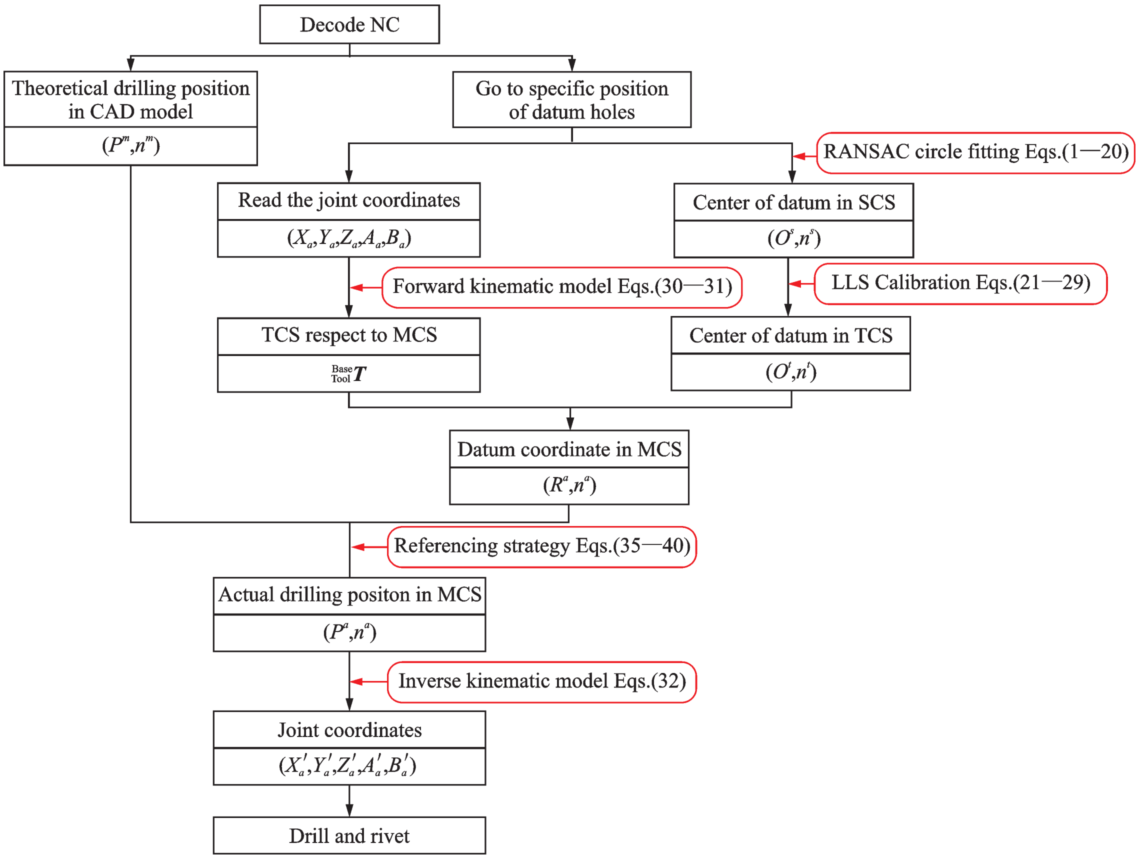

Fig.11 Procedure of referencing

5 Experiments and Verification

5.1 Measuring accuracy

In order to verify the accuracy of the measurement system we established an experimental platform, as shown in Fig.12. The platform consists of ADRS, a test piece on which holes had been drilled, and the Leica laser tracker.

First, the unknown kinematic parameters l_1—l_4 were measured by the laser tracker as l_1= 0.636 mm, l_2= 879.847 mm, l_3= 9.953 mm, and l_4 = 443.271 mm. Then, we used the method described in Section 3.2 to calibrate LLS and obtained ${}_S^T T$ =

$$\begin{bmatrix} 1.0 & -0.004\,42 & 0.002\,91 & 12.498\,5 \\ 0.004\,42 & 1.0 & -0.002\,3 & 277.604 \\ -0.002\,9 & 0.002\,32 & 1.0 & -5.580 \\ 0 & 0 & 0 & 1 \end{bmatrix},$$

and input these parameters into the control software.

Second, we established the TCS by using the method presented in Section 3.1. The datum hole

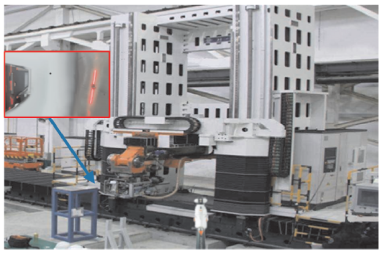

Fig.12 The experiment platform

was placed within the measuring range of LLS. Then, we could obtain the hole's TCS coordinates by TTL, and measured them by the laser trackers as well. By moving the hole, we could collect several measured results, as listed in Table 2, and the results demonstrated that the error in TCS of the measurement system is within 0.1 mm. This high accuracy accounts on the accuracy of LLS, the algorithm of circle fitting, and the calibration process.

Table 2 Accuracy of normal measurement

No.	Laser tracker	LLS	Error/mm	No.	Laser tracker	LLS	Error/mm
1	(5.38, 4.24, 2.61)	(17.86, 281.84, −2.95)	0.02	11	(0.04, 6.33, 0.06)	(12.51, 283.96, −5.52)	0.03
2	(4.84, 5.49, −2.04)	(17.32, 283.09, −7.63)	0.03	12	(−0.70, 5.45, −4.05)	(11.76, 283.07, −9.62)	0.01
3	(3.97, 4.36, −4.37)	(16.43, 281.97, −9.94)	0.04	13	(−1.96, −0.88, 1.29)	(10.57, 276.77, −4.29)	0.06
4	(2.14, −1.29, 1.33)	(14.66, 276.34, −4.26)	0.03	14	(−0.61, −0.09, −2.27)	(11.89, 277.56, −7.83)	0.05
5	(4.92, −1.97, −2.49)	(17.41, 275.66, −8.10)	0.01	15	(−0.12, 0.17, −4.87)	(12.36, 277.79, −10.43)	0.02
6	(2.79, 0.67, −3.03)	(15.27, 278.27, −8.62)	0.06	16	(0.39, −5.54, 3.24)	(12.95, 272.12, −2.34)	0.07
7	(5.27, −5.79, 1.61)	(17.79, 271.86, −4.00)	0.06	17	(−2.04, −4.48, −2.22)	(10.49, 273.18, −7.82)	0.06
8	(3.12, −8.19, −0.04)	(15.67, 269.48, −5.66)	0.05	18	(−2.32, −6.22, −5.05)	(10.21, 271.43, −10.64)	0.05
9	(1.46, −5.78, −5.26)	(13.97, 271.90, −10.85)	0.04	19	(−6.24, 4.79, 1.29)	(6.27, 282.43, −4.29)	0.08
10	(−2.00, 4.01, 0.67)	(10.46, 281.63, −4.91)	0.09	20	(−4.99, 6.53, −0.64)	(7.49, 284.17, −6.18)	0.06

5.2 Referencing accuracy

In order to verify the referencing strategy, we employed a cylindrical part that was similar to an aircraft fuselage, as shown in Fig.13. Its diameter was about 400 mm and its height about 1 500 mm. The datum holes had been drilled in both horizontal and vertical directions, and a series of theoretical positions, generated by offline programming, were evenly distributed between them. Based on these datum holes, the positions of holes to be drilled would be adjusted.

As shown in Fig.14, two criteria were adopted to verify drilling accuracy: the normal error e_n, indicating the distance from the actual drilling hole to the line determined by the two datum holes, and the lengthwise error e_l defined as

$$e_{i_l} = d_i - \frac{1}{n}\sum_{i=1}^{n} d_i \tag{41}$$

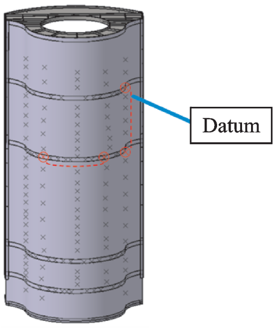

Fig.13 Experiment part

where d_i is the distance between two adjacent holes.

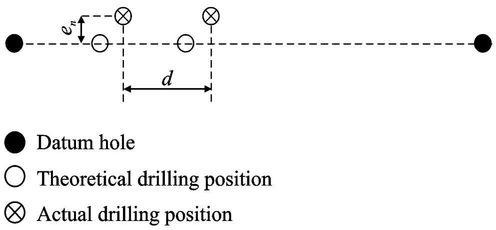

Fig.14 Diagram of precision criteria

Table 3 and Table 4 show the accuracy of a group of holes in horizontal and vertical directions, respectively. It can be seen that the error is less than 0.5 mm, and the errors of holes in horizontal direction is larger than that in vertical direction, because the curvature of product in horizontal direction is larger than that in the vertical direction.

Table 3 Referencing accuracy of holes in horizontal direction mm

No.	e_n	e_l	e	No.	e_n	e_l	e
1	0.23	0.34	0.41	6	0.41	0.06	0.41
2	0.12	0.09	0.15	7	0.13	0.18	0.22
3	0.38	0.18	0.42	8	0.36	0.39	0.46
4	0.32	0.11	0.34	9	0.28	0.13	0.31
5	0.16	0.37	0.40	10	0.17	0.16	0.23

Table 4 Referencing accuracy of holes in vertical direction mm

No.	e_n	e_l	e	No.	e_n	e_l	e
1	0.30	0.12	0.32	6	0.15	0.29	0.33
2	0.26	0.38	0.46	7	0.05	0.21	0.22
3	0.35	0.12	0.37	8	0.18	0.24	0.30
4	0.13	0.36	0.38	9	0.26	0.29	0.39
5	0.25	0.13	0.28	10	0.12	0.41	0.43

6 Conclusions

This paper presents a measuring mechanism that consists of a LLS and a servomotor for the ADRS in aircraft assembly. First, we adopt a RANSAC fitting algorithm to obtain the centers of the holes in 3D space, and devise a method to calibrate LLS. Second, we establish the kinematic model of the machine tool, and clarify the relation between the TCS and the MCS, thus the coordinates of the datum holes in MCS can be measured. Third, we design a two-point referencing strategy to finally adjust the positions of the holes to be drilled.

We also establish an experimental platform to validate our approach. The experimental results indicate that the accuracy of the measuring mechanism is less than 0.2 mm, and the referencing accuracy of the holes after correction is less than 0.5 mm.

We intend to improve the accuracy of our approach, by calibrating the machine tool and collecting more accurate parameters. Also, we would expand the scope of LLS from holes to datum rivets.

References

[1] HEMPSTEAD B, DEVLIEG R, MISTRY R, et al. Drill and drive end effector[C]//2001 Automated Fastening Conference and Exposition.[S.l.]:SAE International, 2001.

[2] LOGEMANN T. Mobile robot assembly cell (RACe) for drilling and fastening[C]//SAE 2016 Aerospace Manufacturing and Automated Fastening Conference and Exhibition.[S.l.]:SAE International, 2016.

[3] BRAHIM NECIB F H. Stress analysis of an aircraft fuselage with and without portholes using CAD/CAE process [J]. Journal of Aeronautics & Aerospace Engineering, 2015, 4(1): 1-8.

[4] GONG M, YUAN P, WANG T, et al. A novel method of surface-normal measurement in robotic drilling for aircraft fuselage using three laser range sensors[C]//2012 IEEE/ASME International Conference on Advanced Intelligent Mechatronics (AIM). [S.l.]:IEEE/ASME, 2012: 450-455.

[5] TIAN W, ZHOU W, ZHOU W, et al. Auto-normalization algorithm for robotic precision drilling system in aircraft component assembly[J]. Chinese Journal of Aeronautics, 2013, 26(2): 495-500.

[6] SHI Z, YUAN P, WANG Q, et al. New design of a compact aero-robotic drilling end effector: An experimental analysis [J]. Chinese Journal of Aeronautics, 2016, 29(4): 1132-1141.

[7] YU L, ZHANG Y, BI Q, et al. Research on surface normal measurement and adjustment in aircraft assembly [J]. Precision Engineering, 2017,50: 482-493.

[8] MEI B, ZHU W, YUAN K, et al. Robot base frame calibration with a 2D vision system for mobile robotic drilling [J]. International Journal of Advanced Manufacturing Technology, 2015,80: 1903-1917.

[9] ZHU W, MEI B, YAN G, et al. Measurement error

analysis and accuracy enhancement of 2D vision system for robotic drilling[J].Robotics and Computer Integrated Manufacturing,2014,30(2): 160-171.

[10] ZHU W D, MEI B, YAN G R, et al. Development of a monocular vision system for robotic drilling [J]. Journal of Zhejiang University SCIENCE C, 2014,15 (8): 593-606.

[11] WANG Z X, BAI J, ZHANG X Y, et al.Base detection research of drilling robot system by using visual inspection[J]. Journal of Robotics, 2018: 1-9.

[12] ZHU W, QU W, CAO L, et al. An off-line programming system for robotic drilling in aerospace manufacturing[J]. International Journal of Advanced Manufacturing Technology, 2013, 68 (9/10/11/12) : 2535-2545.

[13] SUMEIHL H, STURMER B C. Referencing strategies for high accuracy machining of large aircraft components with mobile robotic systems[C]//AeroTech Congress and Wchibition.[S.l.]: SAE International, 2017.

[14] ZHANG Lin, TIAN Wei, LI Dawei, et al. Design of drilling and riveting multifunctional end effector for CFRP and aluminum components in robotic aircraft assembly [J]. Transactions of Nanjing University of Aeronautics and Astronautics, 2018, 35(3), 529-538.

[15] SHE C H, CHANG C C. Design of a generic five-axis postprocessor based on generalized kinematics model of machine tool [J]. International Journal of Machine Tools and Manufacture, 2007, 47(3): 537-545.

Acknowledgements This work was supported by the National Natural Science Foundation of China (No.51875287), the National Defense Basic Scientific Research Program of China (No. JCKY2018605C010) and the National Key Research and Development Program of China (No. 2018YFB1306800).

Authors Dr. **ZHANG Lin** is currently an assistant professor in Nanjing University of Aeronautics and Astronautics (NUAA). His research interests include aircraft automated assembly, CNC technology and precision machining technology. He worked as a visiting scholar in Cranfield University of UK from 2015 to 2016.

Prof. **TIAN Wei** received his Ph. D. degree in Mechanical Manufacture and Automation from Nanjing University of Science and Technology in 2007. He currently works in Nanjing University of Aeronautics and Astronautics and his research interest focuses on aircraft intelligent assembly technology.

Mr. **SUN Hailong** is a research director in AVIC Chengdu Aircraft Industry (Group) Co., Ltd. He has been engaged in the research of advanced technology and equipment for aircraft manufacturing.

Mr. **XUE Qiwei** received M.S.degree in Aerospace Manufacturing from Shenyang Aerospace University in 2016. He is pursuing a master's degree at Nanjing University of Aeronautics and Astronautics.

Mr. **LIU Yangyang** received M.S.degree in Mechanical and Automotive Engineering from Anhui Polytechnic University in 2017. He is pursuing a master's degree at Nanjing University of Aeronautics and Astronautics.

Prof. **LIAO Wenhe** is a professor in School of Mechanical Engineering, Nanjing University of Science and Technology. His research interest focuses on microsatellite aircraft automated assembly and 3D printing.

Author contributions Dr. **ZHANG Lin** contributed to the discussion and background of the study, designed the study proposal and wrote the manuscript. Prof. **TIAN Wei** provided the machine tool experimental platform for this research. Mr. **SUN Hailong** supplied aircraft components for study and their manufacturing process data. Mr. **XUE Qiwei** established the mathematical modals for the study. Mr. **LIU Yangyang** conducted the experiments and analysis and interpreted the results. Prof. **LIAO Wenhe** provided financial support for this research.

Competing interests The authors declare no competing interests.

(Production Editor: Sun Jing)